

A MEMS Thermopile Pirani Sensor Integrated With Composite Nanoforests for Vacuum Monitoring in Semiconductor Equipment

Shaohang Xu, Meng Shi, Ruoyang Huang, Chenchen Zhang, Shaojuan Li, Chengjun Huang, Na Zhou, and Haiyang Mao 

Abstract—In this work, a novel MEMS thermopile Pirani sensor integrated with composite nanoforests (CNFs) is presented. As the CNFs have high porosity and a large surface area to volume ratio (SVR), such a sensor possesses enlarged gas heat conduction. Besides, the surface plasmon resonance (SPR) introduced by the CNFs increases light absorption of the sensor, and the enhanced electromagnetic field of the SPR can effectively convert optical energy into heat energy. Compared with the pristine Pirani sensor without such CNFs, the output voltage of this novel sensor is increased by up to 70.9%, the low detection limit (LDL) of pressure is extended by 300%, and its maximum sensitivity is improved by 68.1%. With these superiorities, the as-prepared Pirani sensor can successfully monitor the vacuum information of different semiconductor manufacturing equipments. Backed up by the CMOS-compatible preparation process of the device, a promising future with diverse scenarios for practical applications is expected.

Index Terms—Composite nanoforests (CNFs), MEMS, Pirani sensors, thermopile, vacuum monitoring.

I. INTRODUCTION

IN INDUSTRY of semiconductor, the chip manufacturing processes require a strict environment to avoid contamination of particles and gases [1], because the existence of

particles may act as masks in etching and may introduce defects into the deposited films, therefore may increase the risks of device failure [2]. Besides, material deposition may be affected by the presence of other gas molecules [3]. This is because the molecules of the material being deposited may collide with the molecules of other gases, which may lead to low adhesion of the deposited films, causing abnormal operation of the devices [4]. Therefore, in order to achieve the best functionality of the facilities and the highest accuracy of the processes, the equipment needs to reach or be kept at a certain vacuum environment [5], [6]. For instance, in the dry etching process to form through silicon vias, the pressure of the etching chamber shall be maintained around 10–20 Pa. In case that the vacuum does not reach the required level, the recipe control becomes difficult; consequently, the wafer may get poorly etched or overetched and may even lead to wafer split [7]. Similarly, during metal sputtering, the chamber pressure shall be pumped down to 10^{-1} Pa; otherwise, the plasma density and sputtering rate could not be precisely controlled, as a result may affect the quality of the metal films and may cause deterioration in device performance [8]. In this sense, sensitive detection and monitoring of chamber pressure are urgently required.

Pirani sensors work depending on the variation of heat conduction under different vacuum conditions, which further causes temperature change of the sensing structure in the device, leading to a different electrical output [9], [10], [11], [12]. As can be noted here, the key factor affecting the performance of Pirani sensors is the heat conduction [13], [14]. In particular, by either increasing the gas heat conduction or reducing the solid heat conduction, the performance of Pirani sensors can be enhanced [15], [16]. Generally, there are three different types of Pirani sensors, namely, those based on thermistors [17], [18], the surface acoustic waves (SAWs) [19], [20], and those based on thermopiles [21], [22]. The thermistor-type Pirani sensors are usually easy to prepare and have a wide choice of sensing materials, including carbon nanotubes (CNTs) [23] and silicon (Si) nanowires [24]. However, these sensors usually have a narrow pressure detection range, which limits their application scenarios. As a competitor, the SAW-type Pirani sensors can achieve a wide pressure detection range; however, their preparation usually requires special piezoelectric materials, such as LiNbO_3 . Besides, those devices sometimes need a relatively

Manuscript received 20 July 2023; revised 12 August 2023; accepted 14 August 2023. Date of publication 29 August 2023; date of current version 22 September 2023. This work was supported in part by the National Natural Science Foundation of China under Grant 62201567, Grant 62022081, and Grant 61974099; in part by the Science Fund for Creative Research Groups of the National Natural Science Foundation of China under Grant 62121005; in part by the Youth Innovation Promotion Association, Chinese Academy of Sciences under Grant 2018153 and Grant 2022117; and in part by the Key-Area Research and Development Program of Guangdong Province under Grant 2019B010117001. The review of this article was arranged by Editor D. J. Young. (Corresponding authors: Haiyang Mao; Na Zhou.)

Shaohang Xu, Meng Shi, Ruoyang Huang, Chengjun Huang, Na Zhou, and Haiyang Mao are with the Institute of Microelectronics of Chinese Academy of Sciences, Beijing 100029, China, and also with the University of Chinese Academy of Sciences, Beijing 100049, China (e-mail: zhouna@ime.ac.cn; maohaiyang@ime.ac.cn).

Chenchen Zhang is with the Institute of Microelectronics of Chinese Academy of Sciences, Beijing 100029, China.

Shaojuan Li is with the Changchun Institute of Optics Fine Mechanics and Physics, Chinese Academy of Sciences, Changchun 130033, China, and also with the University of Chinese Academy of Sciences, Beijing 100049, China.

Color versions of one or more figures in this article are available at <https://doi.org/10.1109/TED.2023.3306318>.

Digital Object Identifier 10.1109/TED.2023.3306318

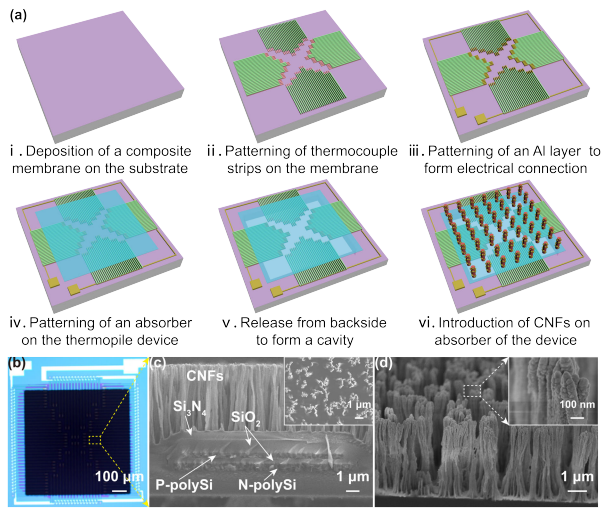


Fig. 1. (a) Fabrication process of the MEMS thermopile Pirani sensor integrated with CNFs. (b) Optical image of the device. (c) and (d) SEM images of the CNFs located on absorber of the thermopile; a thermocouple strip can be seen beneath the CNFs.

complex testing system, and this may add additional costs to the devices [25]. A thermopile-based Pirani sensor consists of a serial connection of multiple thermocouple strips [26]; when compared with the thermistor-type ones, the thermopile-based devices can achieve a larger output signal. Besides, the preparation process and testing system for the thermopile-based Pirani sensors are much simpler than those for the SAW-based sensors. In this view, the thermopile-based Pirani sensors are expected to have wider applications [27] and thus have gained research interest in recent years [28], [29], [30]. However, for practical applications, the sensitivity of conventional thermopile Pirani sensors is still limited and the low-pressure detection limit is not small enough due to the limited gas heat conduction.

To solve these critical issues, in this work, a novel MEMS thermopile Pirani sensor integrated with composite nanoforests (CNFs) is presented. The CNFs exhibit thermal effect because of surface plasmon resonance (SPR), which further enhances the output of the sensor. Moreover, the CNFs also have high porosity and a large surface area-to-volume ratio (SVR), and they provide a superior platform for absorbing gas molecules, thus help to improve the gas heat conduction. With these features, such a Pirani sensor is verified to have a high output, high sensitivity, and a small low detection limit (LDL). With such performance, the device has been successfully adopted to monitor the vacuum information in different manufacturing facilities, indicating significant potential for practical applications.

II. DESIGN AND FABRICATION

Fig. 1(a) illustrates the preparation process for the MEMS thermopile Pirani sensor integrated with CNFs. The process starts with deposition of a composite membrane on a Si substrate, which consists of SiO₂, Si₃N₄, and SiO₂ layers in a sandwich structure for stress compensation. Then, the layers of N-PolySi, SiO₂, P-PolySi, and SiO₂ are deposited, implanted, and patterned successively on the membrane to form thermocouple strips with an isolation layer. After that,

an Al layer (e.g., 500 nm) is sputtered and patterned to form electrodes and the electrical connecting structures. Subsequently, a Si₃N₄ absorber is deposited and patterned on the thermopile. Later on, a back cavity is generated to suspend the composite membrane by using deep reactive ion etching from the backside. After that, a polyimide (PI) layer (e.g., with a thickness of 7 μm) is spin-coated and patterned on the Si₃N₄ absorber. Then, the PI layer is treated with O₂ plasma (e.g., for 25 min) and Ar plasma (e.g., for 20 min), respectively; with this step, nanoforests (NFs) are fabricated on the regions of the PI patterns. Finally, CNFs are obtained by sputtering metal nanoparticles on the NFs. For comparison, a MEMS thermopile Pirani sensor without the CNFs is also prepared at the same time.

Fig. 1(b) shows the optical microscope image of the prepared thermopile Pirani sensor, which is 1.1 × 1.1 mm in size. In the device, the CNFs are patterned on the absorbing area, which is 700 × 700 μm. Fig. 1(c) illustrates a scanning electron microscope (SEM) cross-sectional view of a thermocouple strip covered with a Si₃N₄ absorbing layer and CNFs. In the CNFs, individual nanostructures are with a height of 5 μm and an average diameter of 100 nm. The inset in Fig. 1(c) shows the top views of the CNFs, the average interdistance in the CNFs is around 300 nm, and the density of the CNFs is about 10/μm². As demonstrated in Fig. 1(d), metal nanoparticles are distributed evenly around the nanostructures. The morphology and dimensions of the CNFs indicate that such structures have high porosity and a large SVR, which is crucial for heat conduction and the generation of SPR.

III. RESULTS AND DISCUSSION

For a thermopile device, the output voltage is dependent on temperature difference between the hot ends and the cold ends

$$V = N\alpha\Delta T \quad (1)$$

where N is the number of thermocouple strips, α is the difference of Seebeck coefficient between the two thermocouple materials, and ΔT is the temperature difference between the cold and hot ends. To verify that such a thermopile device can respond to the pressure variation, the device was packaged in a TO39 Can with a gas transmission window, and then, we established an experimental system, as shown in Fig. 2(a). In the experiment, the sensor was placed in an enclosed chamber, in which the vacuum condition was regulated by a pump and a controller, while was monitored by a standard pressure sensor. A dc voltage source was used to apply a stable voltage to the light source; and thus, heat could be provided to the sensor. The light source (EMIRS200-PR) was bought from Nanjing Mcsensors Electronics Ltd., and it has a power rating of 450 mW and can supply light with a wide wavelength range of 2–16 μm. A digital multimeter was used to measure the output voltages of the sensor when the light source was applied with different voltages.

Fig. 2(b) and (c) shows the output voltages of the Pirani sensor at pressures of 10⁵ and 10⁻¹ Pa, when the light source was applied with different voltages. The results imply that either an increment in applied voltage to light source or a decrement in pressure can enhance the output voltage, and

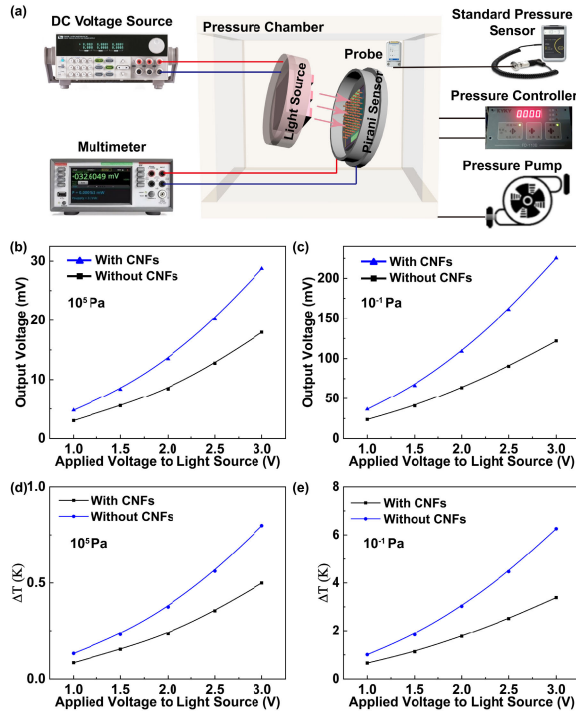


Fig. 2. (a) Schematic of measurement system for the MEMS thermopile Pirani sensors. Output voltages of two Pirani sensors with and without CNFs at chamber pressures of (b) 10^5 and (c) 10^{-1} Pa, when the light source is applied with different voltages. Temperature difference between hot and cold ends of MEMS thermopile Pirani sensors with and without CNFs, when different voltages are applied to light source at chamber pressures of (d) 10^5 and (e) 10^{-1} Pa.

this is because they can increase ΔT . According to (1), ΔT between the hot and cold ends of the MEMS thermopile Pirani sensor can be calculated at different pressures and different applied voltages to light source, as shown in Fig. 2(d) and (e). Here, the number of thermocouple strips N is 100, and the difference of Seebeck coefficient α for the thermocouple strips is $360 \mu\text{V/K}$, and V is the output voltage.

That is to say, such a device is able to detect the vacuum environments. As can also be seen, when compared to its competitor without CNFs, the output of this device is significantly improved, indicating the importance of the CNFs.

The electromagnetic field and heat distributions on the CNFs were simulated by using COMSOL Multiphysics. Fig. 3(a) illustrates a SEM image of an individual CNF structure. According to this image, a model was established for electromagnetic and thermal simulation, as shown in Fig. 3(b). The diameter of individual CNF was 100 nm and that of metal particles was 10 nm. In the simulation, the incident light with a wavelength of $2 \mu\text{m}$ and a power density of $10 \mu\text{W}/\mu\text{m}^2$ propagated along the Z -direction, and periodic boundary conditions were used to perform periodic array in the X - and Y -directions. An ultrafine mesh size of 5 nm was used in all the simulations. Fig. 3(c) and (d) shows the simulation results. As can be seen, the CNFs promote the conversion of optical energy to heat energy and form a heat on the CNFs, which means that CNFs introduce the SPR thermal effect [31].

In order to demonstrate the response of the devices, their output voltages under different vacuum conditions were recorded. Fig. 3(e) illustrates the output of the two devices under different pressures while at a constant voltage (applied to

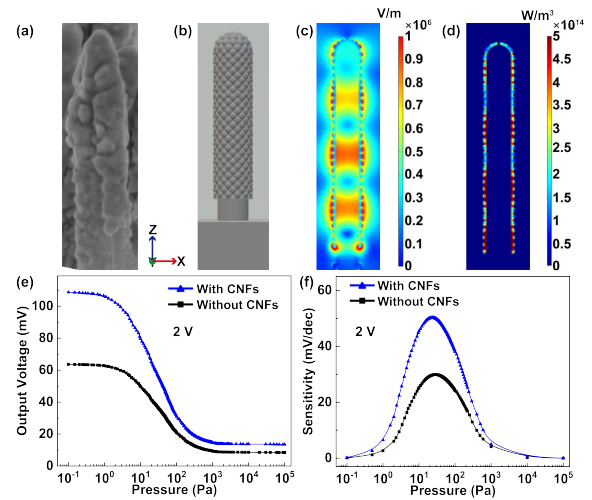


Fig. 3. (a) SEM image and (b) schematic of an individual CNF structure. (c) Electromagnetic field distribution and (d) heat distribution on the CNF structure. (e) Output voltage of the sensors at different pressures. (f) Sensitivity of the sensors versus pressures.

the light source) of 2 V. As can be seen, with the increase of the pressure, the output voltage of the sensors decreases slowly at first; then, there is a sharp decline with the increasing pressure; later, the descending trend of voltage becomes moderate again. This is because when the pressure is very low, only few gas molecules can contribute to heat conduction, and the temperature difference between the cold ends and the hot ends can almost be maintained at its original level. In this situation, the output voltage is also kept at its original level, and the variation is weak. Then, as the pressure increases, more and more gas molecules are involved in heat conduction. In this case, the influence of gas heat conduction becomes more and more obvious. This is because part of the heat at the hot ends tends to dissipate through gas heat conduction. Therefore, the temperature difference between the cold and hot ends is reduced, leading to the decrease of the output voltage. However, when the chamber pressure is approaching the atmosphere, a large number of gas molecules are involved in heat conduction; in such situation, the gas plays the role of a continuous fluid, and the heat flux is independent of the pressure. Therefore, heat dissipation is not affected by the pressure any longer, and thus, the voltage is almost unchanged with the varying pressure.

Meanwhile, as can be observed, the output voltage of the sensor with CNFs is increased by 70.9% when compared to its pristine competitor. The large enhancement can be attributed to the 3-D structures in the CNFs, which can increase absorption by light trapping [32]. In addition, the SPR thermal effect introduced by the CNFs helps to increase the output of the device, as the enhanced electromagnetic field can promote the conversion of optical energy to heat energy. Moreover, the large surface area of the CNFs advances the contact of gas molecules with the sensor; therefore, the slope of this device's output voltage versus pressure is much larger. For such a Pirani sensor, sensitivity S can be defined as the slope of the voltage variation with the logarithm of pressure and can be expressed as follows:

$$S = \frac{\partial V}{\partial (\log_{10} P)} \quad (2)$$

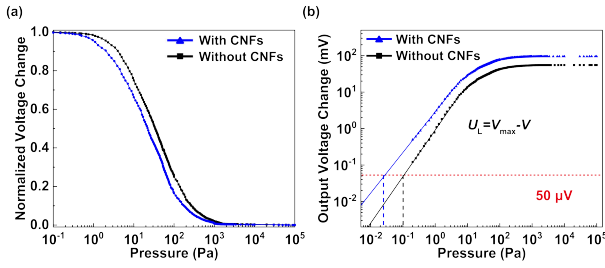


Fig. 4. (a) Normalized voltage changes at different pressures for the MEMS thermopile Pirani sensors. (b) Transfer functions U_L versus pressure for the devices.

TABLE I

PERFORMANCE COMPARISON BETWEEN THE TWO SENSORS WITH AND WITHOUT CNFs

Parameters	Without CNFs	With CNFs	Upgrade
Maximum output voltage (mV)	63.63	108.77	70.9%
Maximum sensitivity (mV/dec)	29.91	50.27	68.1%
LDL (Pa)	10 ⁻¹	2.5×10 ⁻²	300%

where V is the output voltage of the device and P refers to the pressure. Accordingly, the sensitivity of these two sensors is calculated, and the results are demonstrated in Fig. 3(f). As shown in this figure, in a pressure range from 10⁻¹ to 10⁵ Pa, the sensitivity of this novel sensor is substantially enhanced, and a maximum enhancement of 68.1% is achieved at the pressure around 20 Pa.

In order to demonstrate that the novel sensor has superior pressure detection limits compared to its competitor, normalized changes of the output voltages with pressure were calculated, as shown in Fig. 4(a). The results show that when compared with that of the pristine sensor, the curve is left-shifted, indicating that this novel device is more favorable for low-pressure detection and has a smaller LDL, which indicates the minimum pressure that the novel Pirani sensor can detect. To further quantitatively identify the LDLs for both sensors, a transfer function approach is adopted. Here, the transfer function U_L describes the lower pressure limit, which represents the difference between the measured output voltage V at different pressures and the maximum output voltage V_{max} , and it can be expressed as follows:

$$U_L = V_{max} - V. \tag{3}$$

Accordingly, the detectable low-pressure limit of the sensor is defined as the pressure at which the transfer function is equal to the measurement resolution, and the measurement resolution of the voltage is taken as 50 μV, which can be considered as the limit of voltage measurement resolution. Fig. 4(b) shows that when compared to the original device, the novel one extends the LDL toward a smaller value by 300% and reaches 2.5 × 10⁻² Pa, while that is only 10⁻¹ Pa for the competitor. Therefore, the results demonstrate that the integration of CNFs can broaden the low-pressure detection range of the Pirani sensors. Furthermore, other performances of the device have also been improved, as summarized in Table I.

Table II summarizes the performance characteristics of the as-prepared Pirani sensor and other existing devices, indicating that this novel sensor can not only achieve a lower LDL but

TABLE II
PERFORMANCE COMPARISON WITH PREVIOUSLY REPORTED PIRANI SENSORS

Materials	CMOS compatibility	LDL (Pa)	References
CNT	No	0.8	[23]
Si nanowire	Yes	50	[24]
Thermopile	Yes	10	[28]
Thermopile	Yes	1	[29]
Thermopile	Yes	10 ⁻¹	[30]
Thermopile with CNFs	Yes	2.5×10 ⁻²	This work

is also well compatible with CMOS technology and thus can be fabricated in large scale.

Thermopile Pirani sensors work by measuring the heat conduction variation of surrounding gases under different pressure conditions. When a light source supplies heat to the absorber (covering the hot ends) of the thermopile Pirani sensor, while the cold ends are linked with the substrate (kept at a constant temperature), the temperature difference between the hot ends and the cold ends can be determined by the heat loss through the way of gas conduction, which varies with the concentration of gas molecules, namely, the chamber pressure. For a thermopile Pirani sensor, there are three heat transfer routes between the absorber and the substrate: heat conduction, radiation, and thermal convection. Here, the radiation and thermal convection can be neglectable due to the small size and the low operating temperature [33], [34]. On the other hand, for the heat conduction in this sensor, it can be divided into solid heat conduction G_s and gas heat conduction G_g ; here, G_s is independent of pressure, while G_g is a function of pressure.

Fig. 5(a) shows the principle of the gas heat conduction in this sensor. G_g consists of two parts, namely, G_{g1} and G_{g2} ; here, G_{g1} is the heat conduction through the gas molecules on the original Si₃N₄ absorber. While G_{g2} originates from the CNFs, for they have high porosity and a large SVR, which can effectively increase the contacting area for the gas molecules. Therefore, the heat exchange between the sensor and the gas molecules becomes more adequate and consequently leads to increase in gas heat conduction. That is to say, for the pristine sensor, its gas heat conduction $G_g = G_{g1}$, while for this novel device, the gas heat conduction $G_g = G_{g1} + G_{g2}$, which is effectively increased. As a result, the detection range of low pressure is expanded, and the sensitivity is improved. This is because in low-pressure conditions, there are fewer gas molecules, and the increasing G_g is more conducive to the conduction through gas and can more sensitively reflect changes in pressure; thus, it can increase sensitivity and extends the detection range [35], [36].

For the structure proposed in this work, G_g can be expressed as follows:

$$G_g(P) = k_g(P) \frac{A}{d} \tag{4}$$

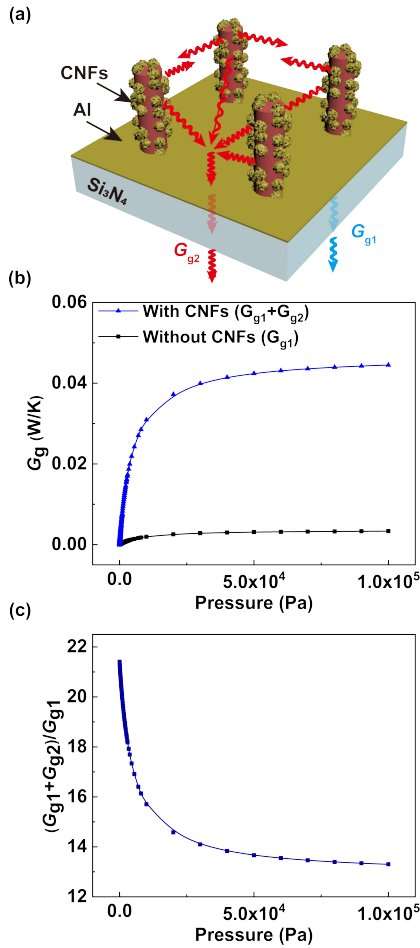


Fig. 5. (a) Principal diagram of gas heat conduction in the MEMS thermopile Pirani sensor integrated with CNFs. (b) Variation of G_g versus pressure. (c) Variation of $(G_{g1} + G_{g2})/G_{g1}$ at different pressures.

where A is the contacting area between the absorber and gas molecules, d is the thickness of the absorber, the values of both A and d change after the integration of CNFs, and k_g is the thermal conductivity of the gas in the chamber, which can be expressed as follows:

$$k_g(P) = k_0 \left(\frac{d}{d + 3.2\lambda(P) \left(\frac{2-\alpha_e}{\alpha_e} \right)} \right) \quad (5)$$

where k_0 is the thermal conductivity of the air at the room temperature and atmospheric pressure, α_e is the energy accommodation coefficient of the molecules, and $\lambda(P)$ is the mean free path of the gas molecules, which can be expressed as follows:

$$\lambda(P) = \frac{k_b T}{\sqrt{2}\pi\sigma^2 P} \quad (6)$$

where k_b is the Boltzmann constant, T is the ambient temperature, and σ is the radius of the gas molecules. According to (4)–(6), the relationship between G_g and the chamber pressure can be obtained as follows:

$$G_g(P) = \frac{0.0259A}{d + \frac{0.0294}{P}} \quad (7)$$

After integration of the CNFs, the contacting area A in the device is enormously increased, the contacting area A_1

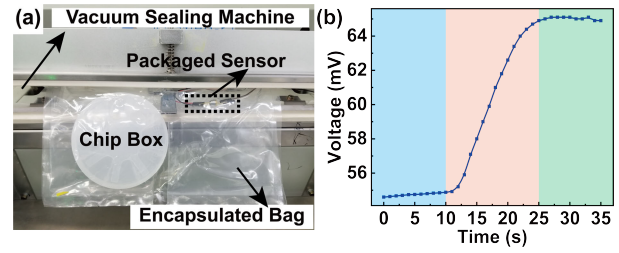


Fig. 6. (a) As-prepared sensor used for monitoring vacuum sealing of a chip box. (b) Output voltage of the sensor in the process of vacuum sealing.

of the pristine device is about $4.9 \times 10^5 \mu\text{m}^2$, and after integrating CNFs, the area (A_2) is increased by about 21 times to $10^7 \mu\text{m}^2$. At the same time, the thickness of the absorber layer d also changes from 3.5 to 6 μm . According to (7), the relations between G_g and pressure are calculated for both sensors, and the results are shown in Fig. 5(b). Owing to the presence of G_{g2} , G_g for the sensor with CNFs is significantly enhanced, and it indicates that at a low pressure, it is more conducive to gas conduction and can be more sensitive to changes in pressure. Therefore, the sensitivity of the novel sensor is also much higher than that of the competitor. In addition, Fig. 5(c) shows the increment of G_g for the novel sensor, which could be calculated by $(G_{g1} + G_{g2})/G_{g1}$. The results demonstrate that the ratio is much greater at a low pressure. This indicates that the sensor with CNFs has a smaller LDL and has a better performance in low-pressure detection.

Owing to the high sensitivity and small LDL, the as-prepared Pirani sensor has promising applications in pressure monitoring, especially in some semiconductor manufacturing-related equipment, including the vacuum sealing machine. Although it is not directly used in the flow of chips, it is extremely important during the transfer of wafers between different manufactories. To monitor the pumping capacity of the vacuum sealing machine, we placed our sensor in a transparent vacuum bag with a 4-in chip box, inside of which there was a quartz wafer, as shown in Fig. 6(a). Then, the pressure inside the package bag during pumping was monitored in real time using the as-prepared sensor. The results are shown in Fig. 6(b), which indicates promising applications of the device in real world. As can be seen in the figure, the output of the sensor changes slowly at first, then, it increases rapidly, and later on, it becomes stable again. Such results show that the vacuum sealing machine pumps slowly at the beginning; and then, the pumping speed becomes faster, thus the output increases rapidly; and finally, the vacuum sealing machine stops working when a certain vacuum level is reached; after that, the package bag is maintained at a fixed vacuum state. Notably, the output of the sensor varies between 54.5 and 65 mV during the entire sealing process, as can be seen in Fig. 3(a) and (b). Such results are nicely corresponding to the high-sensitivity detection range of the as-prepared Pirani sensor. In addition, for a metal sputtering machine, during the metal atom sputtering, the chamber pressure requires to be kept below 10^{-1} Pa, which is out of the reach of conventional Pirani sensors. Since the as-prepared Pirani sensor with CNFs has a proper LDL, thus it has the possibility to be installed in

the chamber for monitoring the vacuum information when it is working.

IV. CONCLUSION

In this work, a MEMS thermopile Pirani sensor with CNFs is designed, fabricated, and tested. The preliminary results demonstrate that the integration of CNFs can effectively enhance the gas heat conduction in the device, and thus, a significant improvement in output voltage, sensitivity, and LDL can be achieved in such a sensor. With these features, the sensor is expected to have further applications in monitoring vacuum information during sputtering and vacuum sealing processes. Since the CNFs as well as the device have the advantages of simple preparation and batch fabrication, the applications of this sensor in real world are expected.

REFERENCES

- [1] K. Nomura, H. Ohta, A. Takagi, T. Kamiya, M. Hirano, and H. Hosono, "Room-temperature fabrication of transparent flexible thin-film transistors using amorphous oxide semiconductors," *Nature*, vol. 432, no. 7016, pp. 488–492, Nov. 2004, doi: [10.1038/nature03090](https://doi.org/10.1038/nature03090).
- [2] W. Shin, S. Hong, Y. Jeong, G. Jung, B.-G. Park, and J.-H. Lee, "Effects of postdeposition annealing ambience on NO₂ gas sensing performance in Si-based FET-type gas sensor," *IEEE Trans. Electron Devices*, vol. 69, no. 5, pp. 2604–2610, May 2022, doi: [10.1109/TED.2022.3161246](https://doi.org/10.1109/TED.2022.3161246).
- [3] T. Tsuchioka et al., "Selective metal deposition on photoswitchable molecular surfaces," *J. Amer. Chem. Soc.*, vol. 130, no. 32, pp. 10740–10747, Aug. 2008, doi: [10.1021/ja802430q](https://doi.org/10.1021/ja802430q).
- [4] S. Osnaghi et al., "Coherent control of an atomic collision in a cavity," *Phys. Rev. Lett.*, vol. 87, no. 3, p. 37902, Jun. 2001, doi: [10.1103/PhysRevLett.87.037902](https://doi.org/10.1103/PhysRevLett.87.037902).
- [5] L. Zhang, J. Lu, H. Takagi, S. Matsumoto, and E. Higurashi, "An ultra-compact MEMS Pirani sensor for in-situ pressure distribution monitoring," *Micromachines*, vol. 13, no. 10, p. 1686, Oct. 2022, doi: [10.3390/mi13101686](https://doi.org/10.3390/mi13101686).
- [6] H. San, Y. Li, Z. Song, Y. Yu, and X. Chen, "Self-packaging fabrication of silicon-glass-based piezoresistive pressure sensor," *IEEE Electron Device Lett.*, vol. 34, no. 6, pp. 789–791, Jun. 2013, doi: [10.1109/LED.2013.2258320](https://doi.org/10.1109/LED.2013.2258320).
- [7] S. Minnikanti, J. Ahn, Y. S. Obeng, and D. R. Reyes, "Generating multiscale gold nanostructures on glass without sidewall deposits using minimal dry etching steps," *ACS Nano*, vol. 13, no. 4, pp. 3924–3930, Apr. 2019, doi: [10.1021/acsnano.8b07004](https://doi.org/10.1021/acsnano.8b07004).
- [8] J. E. Greene, "Review article: Tracing the recorded history of thin-film sputter deposition: From the 1800s to 2017," *J. Vac. Sci. Technol. A, Vac., Surf., Films*, vol. 35, no. 5, p. Sep. 2017, doi: [10.1116/1.4998940](https://doi.org/10.1116/1.4998940).
- [9] G. Gloeckler and H. Ven Horst, "The Pirani gauge," *Science*, vol. 116, no. 3014, pp. 364–367, Oct. 1952, doi: [10.1126/science.116.3014.364](https://doi.org/10.1126/science.116.3014.364).
- [10] J. Lai et al., "Study on fusion mechanisms for sensitivity improvement and measurable pressure limit extension of Pirani vacuum gauges with multi heat sinks," *J. Microelectromech. Syst.*, vol. 29, no. 1, pp. 100–108, Feb. 2020, doi: [10.1109/JMEMS.2019.2954155](https://doi.org/10.1109/JMEMS.2019.2954155).
- [11] E. Gavignet and F. Lanzetta, "Dynamic operation of a micro-thermocouple sensor as a vacuum gauge," *Vacuum*, vol. 100, pp. 18–21, Feb. 2014, doi: [10.1016/j.vacuum.2013.07.043](https://doi.org/10.1016/j.vacuum.2013.07.043).
- [12] W. Xu, X. Wang, X. Pan, A. Bermak, Y.-K. Lee, and Y. Yang, "A wafer-level packaged CMOS MEMS Pirani vacuum gauge," *IEEE Trans. Electron Devices*, vol. 68, no. 10, pp. 5155–5161, Oct. 2021, doi: [10.1109/TED.2021.3103486](https://doi.org/10.1109/TED.2021.3103486).
- [13] K. Jousten, "On the gas species dependence of Pirani vacuum gauges," *J. Vac. Sci. Technol. A, Vac., Surf., Films*, vol. 26, no. 3, pp. 352–359, May 2008, doi: [10.1116/1.2897314](https://doi.org/10.1116/1.2897314).
- [14] F. Völklein and A. Meier, "Microstructured vacuum gauges and their future perspectives," *Vacuum*, vol. 82, no. 4, pp. 420–430, Dec. 2007, doi: [10.1016/j.vacuum.2007.08.001](https://doi.org/10.1016/j.vacuum.2007.08.001).
- [15] Q. Xing, J. Lai, Y. Ye, B. Jiao, and G. Zhang, "An improved physical model considering micro-nano scale effects for numerical simulation of Pirani vacuum gauges," *IEEE Electron Device Lett.*, vol. 43, no. 11, pp. 1985–1988, Nov. 2022, doi: [10.1109/LED.2022.3208840](https://doi.org/10.1109/LED.2022.3208840).
- [16] M. Garg, D. S. Arya, S. Kumar, Y. Chiu, and P. Singh, "Reducing solid conduction in electrothermally driven MEMS Pirani gauge using integrated polymeric thin film," *Appl. Phys. Lett.*, vol. 120, no. 8, pp. 3–8, Feb. 2022, doi: [10.1063/5.0079857](https://doi.org/10.1063/5.0079857).
- [17] D. Lee, Y. Noh, S. Park, M. Kumar, and Y. S. Cho, "Performance enhancement of Pirani gauge on silicon-on-insulator wafer with simple fabrication process," *Sens. Actuators A, Phys.*, vol. 263, pp. 264–268, Aug. 2017, doi: [10.1016/j.sna.2017.06.032](https://doi.org/10.1016/j.sna.2017.06.032).
- [18] E. S. Topalli, K. Topalli, S. E. Alper, T. Serin, and T. Akin, "Pirani vacuum gauges using silicon-on-glass and dissolved-wafer processes for the characterization of MEMS vacuum packaging," *IEEE Sensors J.*, vol. 9, no. 3, pp. 263–270, Mar. 2009, doi: [10.1109/JSEN.2008.2012200](https://doi.org/10.1109/JSEN.2008.2012200).
- [19] P. Nicolay, O. Elmazria, F. Sarry, L. Bouvot, N. Marche, and H. Kambara, "Innovative surface acoustic wave sensor for accurate measurement of subatmospheric pressure," *Appl. Phys. Lett.*, vol. 92, no. 14, pp. 4–5, Apr. 2008, doi: [10.1063/1.2908038](https://doi.org/10.1063/1.2908038).
- [20] P. Nicolay and M. Lenzhofer, "A wireless and passive low-pressure sensor," *Sensors*, vol. 14, no. 2, pp. 3065–3076, Feb. 2014, doi: [10.3390/s140203065](https://doi.org/10.3390/s140203065).
- [21] D. V. Randjelović et al., "Intelligent thermal vacuum sensors based on multipurpose thermopile MEMS chips," *Vacuum*, vol. 101, pp. 118–124, Mar. 2014, doi: [10.1016/j.vacuum.2013.07.044](https://doi.org/10.1016/j.vacuum.2013.07.044).
- [22] M. Pioletto, S. D. Cesta, and P. Bruschi, "A CMOS compatible micro-pirani vacuum sensor based on mutual heat transfer with 5-decade operating range and 0.3 Pa detection limit," *Sens. Actuators A, Phys.*, vol. 263, pp. 718–726, Aug. 2017, doi: [10.1016/j.sna.2017.06.033](https://doi.org/10.1016/j.sna.2017.06.033).
- [23] F. Yu and J. Zhang, "Single-walled carbon nanotube Pirani gauges prepared by DEP assembly," *IEEE Trans. Nanotechnol.*, vol. 12, no. 3, pp. 323–329, May 2013, doi: [10.1109/TNANO.2013.2247623](https://doi.org/10.1109/TNANO.2013.2247623).
- [24] T. Brun, D. Mercier, A. Koumela, C. Marcoux, and L. Duraffourg, "Silicon nanowire based Pirani sensor for vacuum measurements," *Appl. Phys. Lett.*, vol. 101, no. 18, pp. 2010–2014, Oct. 2012, doi: [10.1063/1.4765665](https://doi.org/10.1063/1.4765665).
- [25] K. J. Singh et al., "Enhanced sensitivity of SAW-based Pirani vacuum pressure sensor," *IEEE Sensors J.*, vol. 11, no. 6, pp. 1458–1464, Jun. 2011, doi: [10.1109/JSEN.2010.2086055](https://doi.org/10.1109/JSEN.2010.2086055).
- [26] X. Guo, X. Lu, P. Jiang, and X. Bao, "SrTiO₃/CuNi-heterostructure-based thermopile for sensitive human radiation detection and noncontact human-machine interaction," *Adv. Mater.*, vol. 34, no. 35, 2022, Art. no. 2204355, doi: [10.1002/adma.202204355](https://doi.org/10.1002/adma.202204355).
- [27] A. L. Hsu et al., "Graphene-based thermopile for thermal imaging applications," *Nano Lett.*, vol. 15, no. 11, pp. 7211–7216, Nov. 2015, doi: [10.1021/acs.nanolett.5b01755](https://doi.org/10.1021/acs.nanolett.5b01755).
- [28] S. J. Chen and Y. C. Wu, "A new macro-model of gas flow and parameter extraction for a CMOS-MEMS vacuum sensor," *Symmetry*, vol. 12, no. 10, pp. 1–16, Oct. 2020, doi: [10.3390/sym12101604](https://doi.org/10.3390/sym12101604).
- [29] S.-J. Chen and R.-T. Ding, "Investigation on an active thermoelectric vacuum sensor with low frequency modulation," *IOP Conf. Ser., Mater. Sci. Eng.*, vol. 644, no. 1, Oct. 2019, Art. no. 012024, doi: [10.1088/1757-899X/644/1/012024](https://doi.org/10.1088/1757-899X/644/1/012024).
- [30] C. Lei et al., "A CMOS-MEMS IR device based on double-layer thermocouples," *Microsyst. Technol.*, vol. 22, no. 5, pp. 1163–1171, May 2016, doi: [10.1007/s00542-015-2688-z](https://doi.org/10.1007/s00542-015-2688-z).
- [31] V. Amendola, R. Pilot, M. Frascioni, O. M. Maragò, and M. A. Iatì, "Surface plasmon resonance in gold nanoparticles: A review," *J. Phys., Condens. Matter*, vol. 29, no. 20, May 2017, Art. no. 203002, doi: [10.1088/1361-648X/aa60f3](https://doi.org/10.1088/1361-648X/aa60f3).
- [32] M. Li et al., "Quasi-ordered nanoforests with hybrid plasmon resonances for broadband absorption and photodetection," *Adv. Funct. Mater.*, vol. 31, no. 38, Sep. 2021, Art. no. 2102840, doi: [10.1002/adfm.202102840](https://doi.org/10.1002/adfm.202102840).
- [33] F. T. Zhang, Z. Tang, J. Yu, and R. C. Jin, "A micro-pirani vacuum gauge based on micro-hotplate technology," *Sens. Actuators A, Phys.*, vol. 126, no. 2, pp. 300–305, Feb. 2006, doi: [10.1016/j.sna.2005.10.016](https://doi.org/10.1016/j.sna.2005.10.016).
- [34] X. Sun, D. Xu, B. Xiong, G. Wu, and Y. Wang, "A wide measurement pressure range CMOS-MEMS based integrated thermopile vacuum gauge with an XeF₂ dry-etching process," *Sens. Actuators A, Phys.*, vol. 201, pp. 428–433, Oct. 2013, doi: [10.1016/j.sna.2013.07.020](https://doi.org/10.1016/j.sna.2013.07.020).
- [35] G.-J. Jeon, W. Y. Kim, H. B. Shim, and H. C. Lee, "Nanoporous Pirani sensor based on anodic aluminum oxide," *Appl. Phys. Lett.*, vol. 109, no. 12, Sep. 2016, doi: [10.1063/1.4963183](https://doi.org/10.1063/1.4963183).
- [36] S. Guo et al., "Design of a high sensitivity Pirani gauge based on vanadium oxide film for high vacuum measurement," *Sensors*, vol. 22, no. 23, p. 9275, Nov. 2022, doi: [10.3390/s22239275](https://doi.org/10.3390/s22239275).